A fatigue model under Cosserat peridynamic framework for concrete fatigue cracking

Xianyang Guo[1], Ji Wan[1], Xihua Chu[1,*], Shan Li [1]

1: School of Civil Engineering, Wuhan University, Wuhan, 430072, China.

* Corresponding author,

E-mail: chuxh@whu.edu.cn

ABSTRACT

A novel fatigue model under Cosserat peridynamic framework is proposed to investigate concrete fatigue performance. In this model, a novel cyclic bond failure criterion is established to measure the combined tension/compressive-shear fatigue failure in concrete, which is derived from the Bresler-Pister criterion. Three benchmarks with different fatigue crack modes in concrete are designed. Results show that the mode I and mixed mode I-II fatigue crack patterns are predicted. In the three-point-bend beam fatigue test, the numerical result matches well with the experimental result, in the uniaxial compressive fatigue test, the effects of Cosserat parameters on fatigue crack patterns are discussed. Results found that the Cosserat parameters reflect the effects of concrete microstructures on crack patterns, and the larger Cosserat shear modulus accelerates the fatigue crack propagation process.

KEYWORDS: Cyclic bond failure criterion; Concrete fatigue failure; Cosserat peridynamic model; Crack propagation.

1. Introduction

Concrete infrastructure facilities exist throughout the industrial production and living activities of human beings. In concrete facilities, fatigue failure is one of the main failure modes (Chaboche and Lesne, 1988, Sun and Xu, 2021). Due to the cyclic loads, the minor existing imperfection expands (Cachim, et al., 2002) and forms macroscopic cracks, which increases the possibility of accidents. Hence, it is prominent to investigate the fatigue performance and crack patterns in concrete materials.

To describe the concrete fatigue performance, a series of empirical methods are proposed: Aas-Jakobsen (Aas-Jakobsen, 1970) proposed the concrete S-N curve to correspond fatigue life with stress levels, the concrete S-N curve was extended in the following research (Tepfers and Kutti, 1979, Hsu, 1981, Saucedo, et al., 2013); Baluch et al. (Baluch, et al., 1989) and Perdikaris et al. (Perdikaris and Calomino, 1989) proposed the concrete Paris law to describe fatigue crack growth, the concrete Paris law was modified in subsequent studies (Forman, et al., 1967, Elber, 1970, Klesnil and Lukáš, 1972, Priddle, 1972, Bazant and Xu, 1991, Sain and Kishen, 2008, Carpinteri, et al., 2010, Ray and Kishen, 2011, Ray and Chandra Kishen, 2012). Besides, based on fracture mechanics, the cohesive crack model for concrete fatigue failure was proposed and developed by the following works (Hillerborg, et al., 1976, Hordijk, 1993, Yang, et al., 2001), which deal with a single crack (Ding, et al., 2019); based on damage mechanics, researchers (Marigo, 1985, Papa and Taliercio, 1996, Mai, et al., 2012) established the damage evolution law to deal with concrete fatigue failure. Notice that the crack growth rate equations (McEvily and Wei, 1972, Pearson, 1972, Branco, et al., 1975, Miller, 1993) are appropriate for fatigue problems. However, most of the existing crack growth rate equations focus on metal materials such as steel and aluminum alloy (Forman, et al., 1967, Elber, 1970, Klesnil and Lukáš, 1972, McEvily and Wei, 1972, Pearson, 1972, Priddle, 1972, Branco, et al., 1975, Miller, 1993).

With the development of computer science, several numerical methods are applied to investigate concrete fatigue failure such as the finite element method (FEM) (Pryl, et al., 2014, Lesiuk, et al., 2020, Wang, et al., 2020, Sun and Xu, 2021), and continuum

damage mechanics (CDM) (Maitra, et al., 2014, Ding and Li, 2018, Ding, et al., 2019, Wu, et al., 2019). However, these approaches within the continuum mechanics encounter difficulties in dealing with discontinuity problems, and extra criteria are introduced.

Peridynamics (PD) is a nonlocal continuum theory proposed by Silling (Silling, 2000). In PD, the body is divided into material points containing volume and mass, the material points interact with others within a specific range. The motion equations are rewritten with integrals instead of differentials to deal with discontinuous problems (Wan, et al., 2020, Chen and Chu, 2021, Chen and Chu, 2022, Chen, et al., 2022, Feng and Zhou, 2022). Bond-based PD (BPD) is a traditional peridynamic model, in which the interactions between material points are called bonds (Guo, et al., 2021). In BPD, the Poisson's ratio is limited due to the one parameter describing micro elastic bond stretch response. To deal with the limitation, state-based peridynamics (SPD) (Breitenfeld, et al., 2014, Madenci and Oterkus, 2016) and several extended bond-based peridynamics (EBPD), which contain multiple elastic parameters, were proposed (Gerstle, et al., 2007, Prakash and Seidel, 2015, Yaghoobi and Chorzepa, 2017, Zhu and Ni, 2017, Zhou, et al., 2018, Chen, et al., 2019, Diana and Casolo, 2019, Huang, et al., 2019, Gu and Zhang, 2020). In the latest work of Diana (Diana, 2022), the revised bond-based peridynamic theory with oriented material points is proposed to deal with anisotropic elasticity, fracture and diffusion-type problems, in which a consistent micro-macro moduli correspondence between material parameters of anisotropic peridynamics and classical continuum physics is established.

To investigate the fatigue performance of metal materials, based on BPD, Silling and Askari (Silling and Askari, 2014) proposed a peridynamic model for fatigue cracking, the remaining life of the bond is introduced, which relates to the cyclic bond strain. Based on Silling's work (Silling and Askari, 2014), several extended peridynamic models for fatigue cracking are proposed (Zhang and Bobaru, 2016, Zhang, et al., 2016, Hu and Madenci, 2017, Jung and Seok, 2017, Nguyen, et al., 2021) Han et al. (Han and Chen, 2020) proposed an alternative ordinary state-based peridynamic model for fatigue cracking. Ni et al. (Ni, et al., 2023) proposed a bond-based

peridynamic model to simulate fatigue crack propagation in composite materials and structures. Notice that most of the existing PD fatigue models focus on metal materials like aluminum alloy (Sajith, et al., 2020, Bang, et al., 2021, Bang and Ince, 2022, Li, et al., 2022), and few have proposed PD fatigue models for concrete. Due to the difference in the mechanical properties between metal and concrete, those existing PD fatigue models cannot be directly applied to investigate concrete fatigue failure.

Under Cosserat peridynamic framework, this study proposes a novel fatigue model for concrete fatigue cracking (F-CPD). In this model, a novel cyclic bond failure criterion is established to measure the combined tension/compressive-shear fatigue failure in concrete, which is derived from the Bresler-Pister criterion (Bresler and Pister, 1958). The novel concrete fatigue failure model consists of three phases: the crack nucleation phase (phase I), the crack growth phase (phase II), and the rapid crack growth phase (phase III). In phase I, the fatigue iteration parameters are derived from the traditional concrete S-N curve proposed by Aas-Jakobsen (Aas-Jakobsen, 1970); in phase II, the fatigue iteration parameters are derived from the concrete Paris law modified by Bazant (Bazant and Xu, 1991); in phase III, the static bond failure criterion is proceeded. Three concrete fatigue failure benchmarks with different loading conditions are designed. In the three-point-bend beam fatigue test, the numerical result matches well with the experimental result; in the uniaxial compressive fatigue test, the effects of Cosserat parameters on fatigue crack patterns are discussed; In the biaxial compressive concrete fatigue test, a discussion of the effect of confining pressure on fatigue crack is performed.

This study is constructed as follows: Section 2 introduces the peridynamic theory and the Cosserat peridynamic model; Section 3 introduces the novel fatigue model under Cosserat peridynamic framework for concrete fatigue cracking; Section 4 shows three benchmarks: the fatigue test of a three-point-bend beam, the uniaxial compressive concrete fatigue test, and the biaxial compressive concrete fatigue test; Section 5 presents the summary and conclusions.

2. Peridynamic theory

2.1. Bond-based Peridynamic theory

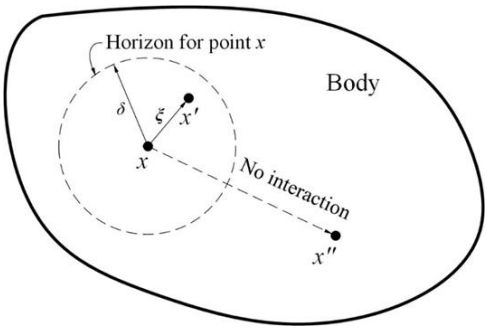

FIGURE 1. Material point interacts with others within its peridynamic horizon (Guo, et al., 2021).

In BPD, a material point **x** interacts with others through fictitious bonds within a specific range named horizon, noted by δ. We conventionally denote $H_x=\{\mathbf{x}'\big|\big|\mathbf{x}'-\mathbf{x}\big|<\delta\}$. The kinematic equation of material point x at time t is expressed as:

$$\rho\ddot{\mathbf{u}}(\mathbf{x},t)=\int_{H_x}\mathbf{f}\left(\mathbf{u}(\mathbf{x}',t)-\mathbf{u}(\mathbf{x},t),\mathbf{x}'-\mathbf{x}\right)\mathrm{d}V'+\mathbf{b}(\mathbf{x},t) \tag{1}$$

In which ρ is the density, **u** denotes the displacement vector field, **b** denotes the prescribed body force density field, and **f** denotes the pairwise force function, whose value is the force vector per unit volume squared. The relative position in the reference configuration $\boldsymbol{\xi}$ is given as:

$$\boldsymbol{\xi}=\mathbf{x}'-\mathbf{x} \tag{2}$$

The relative displacement $\boldsymbol{\eta}$ is denoted as:

$$\boldsymbol{\eta}=\mathbf{u}(\mathbf{x}',t)-\mathbf{u}(\mathbf{x},t) \tag{3}$$

$\boldsymbol{\xi}+\boldsymbol{\eta}$ denotes the current relative position vector. According to Silling's research (Silling and Askari, 2005), the general form of **f** is expressed as:

$$\mathbf{f}(\boldsymbol{\eta},\boldsymbol{\xi})=\frac{\boldsymbol{\xi}+\boldsymbol{\eta}}{|\boldsymbol{\xi}+\boldsymbol{\eta}|}f\left(y(t),\boldsymbol{\xi},t\right)\quad\forall\boldsymbol{\xi},\boldsymbol{\eta} \tag{4}$$

where f represents the scalar bond force, and y denotes the current relative position:

$$y=|\boldsymbol{\xi}+\boldsymbol{\eta}| \tag{5}$$

With Equation (5), the relative bond stretch s is defined as:

$$s=\frac{|\boldsymbol{\xi}+\boldsymbol{\eta}|-|\boldsymbol{\xi}|}{|\boldsymbol{\xi}|}=\frac{y-|\boldsymbol{\xi}|}{|\boldsymbol{\xi}|} \tag{6}$$

Considering a prototype micro elastic brittle (PMB) material (Silling and Askari, 2005), f is defined as:

$$f(y(t),\boldsymbol{\xi})=\mu_0(t,\boldsymbol{\xi})cs \tag{7}$$

in which c represents micro-modulus. A notion μ_0 is introduced to predict bond breaking, which is a history-dependent damage function:

$$\mu_0(t, \boldsymbol{\xi})=\begin{cases}1 & \text{if } s(t, \boldsymbol{\xi})< s_{\mathrm{c}} \quad \forall 0\leq t\leq t' \\ 0 & \text{otherwise}\end{cases} \tag{8}$$

where s_{c} represents the critical bond stretch. The local damage index $\varphi(\mathbf{x}, t)$ at material point $\mathbf{x}$ is defined as:

$$\varphi(\mathbf{x}, t)=1-\frac{\int_{H\mathbf{x}}\mu_0(\mathrm{x}, t, \boldsymbol{\xi})\mathrm{d}V_{\xi}}{\int_{H\mathbf{x}}\mathrm{d}V_{\xi}} \tag{9}$$

where $0\leq\varphi\leq 1$, $\varphi(\mathbf{x}, t)=0$ means the virgin state, and $\varphi(\mathbf{x}, t)=1$ means all the bonds connected to material point $\mathbf{x}$ are broken.

The micro-modulus c is calculated by comparing and equating the strain energy density distribution under isotropic extension (Silling and Askari, 2005):

$$c=\begin{cases}\dfrac{6E}{\pi(1-\nu)\delta^3 t_{\mathrm{h}}} & \text{in plane stress problem} \\ \dfrac{6E}{\pi(1+\nu)(1-2\nu)\delta^3 t_{\mathrm{h}}} & \text{in plane strain problem} \\ \dfrac{18\kappa}{\pi\delta^4} & \text{in 3D and plane strain problem}\end{cases} \tag{10}$$

where E represents the elasticity modulus, ν represents Poisson's ratio, t_{h} denotes the thickness in the plane stress problem.

2.2. Cosserat peridynamics in 2D conditions

Concrete is a granular material bonded by aggregates of sand and gravel or crushed rock [63], which complicates the microstructures and micro-rotations. The traditional Cauchy continuum cannot describe the micro-rotations accurately, nor can it investigate the size effects of concrete microstructures. The Cosserat continuum considers the independent rotation degree of freedoms (DOFs) and the couple stresses, and the Cosserat parameters related to microstructure (Tang and Hu, 2017) are introduced. Hence, the Cosserat theory is appropriate to describe concrete's mechanical behavior and size effects (Trovalusci and Masiani, 2003, Trovalusci, et al., 2015). Different from the Cauchy continuum, the Cosserat continuum considers the microstructure of matter and independent rotational DOFs, and each material point has three DOFs:

$$\mathbf{u}=[u_x, u_y, \omega_z]^{\mathrm{T}}, \tag{11}$$

where u_x and u_y represent the translational DOFs and ω_z represents the rotational DOF. The stress and strain vectors are defined as follows:

$$\sigma = [\sigma_{xx},\ \sigma_{yy},\ \sigma_{zz},\ \sigma_{xy},\ \sigma_{yx},\ m_{zx}/l_{\mathrm{c}},\ m_{zy}/l_{\mathrm{c}}]^{\mathrm{T}}, \tag{12}$$

$$\varepsilon = [\varepsilon_{xx},\ \varepsilon_{yy},\ \varepsilon_{zz},\ \varepsilon_{xy},\ \varepsilon_{yx},\ \kappa_{zx}l_{\mathrm{c}},\ \kappa_{zy}l_{\mathrm{c}}]^{\mathrm{T}}, \tag{13}$$

where κ_{zx} and κ_{zy} denote micro-curvatures, m_{zx} and m_{zy} denote couple-stresses, l_{c} represents internal length, which relates to microstructures.

The Cosserat peridynamics (CPD) proposed by Chen et al. (Chen, et al., 2019) and Guo et al. (Guo, et al., 2021) is proven to successfully predict the mode II crack, and the convergence of CPD is verified in Chen's work (Chen, et al., 2019). Compared with BPD, the Cosserat peridynamics can capture the micro-curvatures and couple-stresses, which reflects the micro-rotations in concrete granular and solves the limitation of Poisson's ratio. Take the plane stress condition for example. The strain energy density w is written as:

$$w = \frac{1}{2}\left(\sigma_{xx}\varepsilon_{xx}+\sigma_{yy}\varepsilon_{yy}+\sigma_{xy}\varepsilon_{xy}+\sigma_{yx}\varepsilon_{yx}+m_{zx}\kappa_{zx}+m_{zy}\kappa_{zy}\right) \tag{14}$$

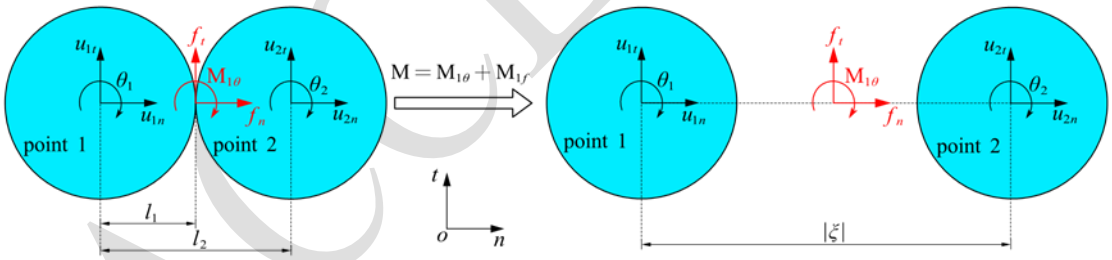

FIGURE 2. Interaction between material points in CPD refers to the discrete element method (DEM) interaction form. M_{1f} denotes the moment from the transverse force f_{1t}, $\mathrm{M}_{1\theta}$ denotes the moment from micro-rotation. ($\mathrm{M} = \mathrm{M}_{1\theta} + \mathrm{M}_{1f}$)

In CPD, the pairwise force can be divided into transverse and axial directions, see **FIGURE 2**:

$$f_{1\mathrm{n}} = k_{\mathrm{n}}(u_{2\mathrm{n}} - u_{1\mathrm{n}}) \tag{15}$$

$$f_{1\mathrm{t}} = k_{\mathrm{t}}(u_{2\mathrm{t}} - u_{1\mathrm{t}}) + k_{\mathrm{t}} \cdot l_{\mathrm{d}}(\theta_1 + \theta_2) \tag{16}$$

where $f_{1\mathrm{n}}$, $f_{1\mathrm{t}}$ are axial and transverse components of pairwise force; k_{n}, k_{t} denote

stiffness coefficients; u_{in}, u_{it} (i=1, 2) denote displacement elements; θ_i (i=1, 2) denote the rotation components. The pairwise moments arise from rotation and transverse forces, which are defined as follows:

$$M_{1\theta} = k_r \cdot (\theta_2 - \theta_1) \tag{17}$$

$$M_{1f} = f_{1t} \cdot l_d = k_t \cdot l_d (u_{2t} - u_{1t}) + k_t \cdot l_d^2 (\theta_1 + \theta_2) \tag{18}$$

$$M = M_{1\theta} + M_{1f} = k_r \cdot (\theta_2 - \theta_1) + k_t \cdot l_d (u_{2t} - u_{1t}) + k_t \cdot l_d^2 (\theta_1 + \theta_2) \tag{19}$$

With Equations (15)-(19), the matrix form of pairwise forces and displacement is written as:

$$\begin{Bmatrix} f_{1n} \\ f_{1t} \\ M_1 \\ f_{2n} \\ f_{2t} \\ M_2 \end{Bmatrix} = \begin{bmatrix} -\frac{k_n}{r} & 0 & 0 & \frac{k_n}{r} & 0 & 0 \\ 0 & -\frac{k_t}{r^3} & \frac{k_t}{r^3} \cdot l_d & 0 & \frac{k_t}{r^3} & \frac{k_t}{r^3} \cdot l_d \\ 0 & -\frac{k_t}{r^3} \cdot l_d & \frac{k_t}{r^3} \cdot l_d^2 - k_r & 0 & \frac{k_t}{r^3} \cdot l_d & \frac{k_t}{r^3} \cdot l_d^2 + k_r \\ \frac{k_n}{r} & 0 & 0 & -\frac{k_n}{r} & 0 & 0 \\ 0 & \frac{k_t}{r^3} & \frac{k_t}{r^3} \cdot l_d & 0 & -\frac{k_t}{r^3} & \frac{k_t}{r^3} \cdot l_d \\ 0 & \frac{k_t}{r^3} \cdot l_d & \frac{k_t}{r^3} \cdot l_d^2 + k_r & 0 & -\frac{k_t}{r^3} \cdot l_d & \frac{k_t}{r^3} \cdot l_d^2 - k_r \end{bmatrix} \cdot \begin{Bmatrix} u_{1n} \\ u_{1t} \\ \theta_1 \\ u_{2n} \\ u_{2t} \\ \theta_2 \end{Bmatrix} \tag{20}$$

The force component from material point 1 to material point 2 is omitted by rewriting Equation (20) with relative displacements ($\hat{u} = u_{2n} - u_{1n}$, $\hat{v} = u_{2t} - u_{1t}$):

$$\begin{Bmatrix} f_{1n} \\ f_{1t} \\ M_1 \end{Bmatrix} = \begin{bmatrix} \frac{k_n}{r} & 0 & 0 & 0 \\ 0 & \frac{k_t}{r^3} & -\frac{k_t}{r^3} \cdot l_d & -\frac{k_t}{r^3} \cdot l_d \\ 0 & -\frac{k_t}{r^3} \cdot l_d & \frac{k_t}{r^3} \cdot l_d^2 - k_r & \frac{k_t}{r^3} \cdot l_d^2 + k_r \end{bmatrix} \cdot \begin{Bmatrix} \hat{u} \\ \hat{v} \\ \theta_1 \\ \theta_2 \end{Bmatrix} \tag{21}$$

Where $w_c(x, y)$ represents the strain energy density. $\{\mathbf{F}\}_\mathbf{c}$, $\{\boldsymbol{u}\}_\mathbf{c}$, $[\mathbf{K}]_\mathbf{c}$ are defined as the PD force components, material point displacements, and stiffness matrix, respectively:

$$\{\mathbf{F}\}_\mathbf{c} = [\mathbf{K}]_\mathbf{c} \cdot \{\boldsymbol{u}\}_\mathbf{c} \tag{22}$$

In CPD, the calculation of strain energy $w_c(x, y)$ at point (x, y) is derived by adding half of every bond's energy to the point (x, y):

$$w_c(x, y) = \frac{1}{4} t_h \iint_{H^*} \{\mathbf{F}\}_\mathbf{c}^\mathbf{T} \cdot \{\boldsymbol{u}\}_\mathbf{c} ds = \frac{1}{4} t_h \int_0^{2\pi} \left(\int_0^{\delta} \{\mathbf{F}\}_\mathbf{c}^\mathbf{T} \cdot \{\boldsymbol{u}\}_\mathbf{c} \, dr \right) d\theta \tag{23}$$

where t_h is the thickness of the plate, ds is the area differential, r is the radius, and θ is the rotation.

The transformation matrix $\boldsymbol{Q}$ is introduced to transform the PD force-displacement relation from local coordinates to global coordinates:

$$\{\mathbf{F}\}_{\mathbf{g}}=\boldsymbol{Q}^{\mathbf{T}}\cdot[\mathbf{K}]_{\mathbf{c}}\cdot\boldsymbol{Q}\cdot\{\boldsymbol{u}\}_{\mathbf{g}} \tag{24}$$

Where $\boldsymbol{Q}$ is expressed as:

$$\boldsymbol{Q}=\begin{bmatrix}\cos\theta & \sin\theta & 0 & 0\\ -\sin\theta & \cos\theta & 0 & 0\\ 0 & 0 & 1 & 0\\ 0 & 0 & 0 & 1\end{bmatrix} \tag{25}$$

The strain energy $w_{\mathrm{g}}(\mathrm{x},\mathrm{y})$ in global coordinates is written as:

$$w_{\mathrm{g}}(\mathrm{x},\mathrm{y})=\frac{1}{4}t_{\mathrm{h}}\int_0^{2\pi}\left(\int_0^{\delta}\{\boldsymbol{u}\}_{\mathbf{g}}{}^{\mathbf{T}}\cdot\boldsymbol{Q}^{\mathbf{T}}\cdot[\mathbf{K}]_{\mathbf{c}}\cdot\boldsymbol{Q}\cdot\{\boldsymbol{u}\}_{\mathbf{g}}\,\mathrm{d}r\right)\mathrm{d}\theta \tag{26}$$

Comparing Equation (26) with Equation (14), the material parameters are derived:

$$k_{\mathrm{n}}=\frac{6E}{t_{\mathrm{h}}\pi\delta^3(1-\mu)} \tag{27}$$

$$k_{\mathrm{t}}=\frac{2E(1-3\mu)}{t_{\mathrm{h}}\pi\delta(1-\mu^2)} \tag{28}$$

$$l_{\mathrm{d}}=\sqrt{\frac{G_{\mathrm{c}}(1-\mu^2)}{2E(1-3\mu)}}\delta \tag{29}$$

$$k_{\mathrm{r}}=\frac{4G_{\mathrm{c}}}{\mathrm{t}\pi\delta^2}-\frac{16Gl_{\mathrm{c}}{}^2}{\mathrm{t}\pi\delta^4} \tag{30}$$

Finally, $[\mathbf{K}]_{\mathbf{c}}$ in Equation (26) is expressed as:

$$\begin{bmatrix}\frac{6E}{t_{\mathrm{h}}\pi\delta^3(1-\mu)}\cdot\frac{1}{r} & 0 & 0 & 0\\ 0 & \frac{2E(1-3\mu)}{t_{\mathrm{h}}\pi\delta(1-\mu^2)}\cdot\frac{1}{r^3} & -\sqrt{\frac{2G_{\mathrm{c}}E(1-3\mu)}{1\text{-}\mu^2}}\cdot\frac{1}{t_{\mathrm{h}}\pi}\cdot\frac{1}{r^3} & -\sqrt{\frac{2G_{\mathrm{c}}E(1-3\mu)}{1-\mu^2}}\cdot\frac{1}{t_{\mathrm{h}}\pi}\cdot\frac{1}{r^3}\\ 0 & -\sqrt{\frac{2G_{\mathrm{c}}E(1-3\mu)}{1-\mu^2}}\cdot\frac{1}{t_{\mathrm{h}}\pi}\cdot\frac{1}{r^3} & \frac{G_{\mathrm{c}}\cdot\delta}{t_{\mathrm{h}}\pi}\cdot\frac{1}{r^3}-\frac{4G_{\mathrm{c}}}{t_{\mathrm{h}}\pi\delta^2}+\frac{16Gl_{\mathrm{c}}{}^2}{t_{\mathrm{h}}\pi\delta^4} & \frac{G_{\mathrm{c}}\cdot\delta}{t_{\mathrm{h}}\pi}\cdot\frac{1}{r^3}+\frac{4G_{\mathrm{c}}}{t_{\mathrm{h}}\pi\delta^2}-\frac{16Gl_{\mathrm{c}}{}^2}{t_{\mathrm{h}}\pi\delta^4}\end{bmatrix} \tag{31}$$

As for the relationship between Cosserat internal length l_{c} and peridynamic horizon, according to Chen's work (Chen and Chu, 2021), the Cosserat internal length l_{c} has an upper limit, and the Cosserat shear modulus G_{c} has a lower limit: $l_{\mathrm{c}}\leq\sqrt{\frac{G_{\mathrm{c}}}{4G}}\cdot\delta$, $G_{\mathrm{c}}\geq\frac{4l_{\mathrm{c}}^2}{\delta^2}\cdot G$. Hence, the Cosserat internal length l_{c} and G_{c} will affect the lower bound of peridynamic length scale δ.

3. Fatigue model under Cosserat peridynamic framework

3.1. Fatigue model under Bond-based peridynamic framework.

Silling et al. (Silling and Askari, 2014) proposed a peridynamic model for fatigue

cracking (F-BPD), which focuses on the fatigue performance of the aluminum alloy. In F-BPD, the fatigue failure process is divided into three phases: the crack nucleation phase (phase I), the crack growth phase (phase II), and the rapid crack growth phase (phase III). The cyclic bond strain ε_{ij}^{N} between material points i and j at a specific loading cycle N is defined as:

$$\varepsilon_{ij}^{N}=\left|s_{ij}^{+}-s_{ij}^{-}\right|=\left|s_{ij}^{+}(1-R)\right| \tag{32}$$

Where s_{ij}^{+}, s_{ij}^{-} represent bond stretch corresponding to the maximum load $\mathrm{P_{max}}$ and $\mathrm{P_{min}}$, respectively. R is the load ratio (R=$\mathrm{P_{max}}$/$\mathrm{P_{min}}$).

For each bond, the remaining life $\lambda\ (x, \xi, N)$ is defined as:

$$\lambda=\begin{cases}\lambda_{ij}^{N=0}=1, & \dfrac{d\lambda_{ij}^{N}}{dN}=-\mathrm{A_1}\left(\varepsilon_{ij}^{N}\right)^{\mathrm{m_1}} \text{ when } \mathrm{A_1}>0,\ \mathrm{m_1}>0 \text{ for phase I}\\ \lambda_{ij}^{N=0}=1, & \dfrac{d\lambda_{ij}^{N}}{dN}=-\mathrm{A_2}\left(\varepsilon_{ij}^{N}\right)^{\mathrm{m_2}} \text{ when } \mathrm{A_2}>0,\ \mathrm{m_2}>0 \text{ for phase II}\end{cases} \tag{33}$$

Where $\mathrm{A_1}$, $\mathrm{m_1}$, $\mathrm{A_2}$, $\mathrm{m_2}$ are fatigue iteration parameters. In phase I, consider a bond ξ_1 has the largest cyclic bond strain ε_1 in the body, the bond ξ_1 will first be broken, compute the corresponding cycle N_1:

$$N_1=\frac{1}{\mathrm{A_1}\varepsilon_1^{\mathrm{m_1}}} \tag{34}$$

Take the log of both sides of Equation (34):

$$\log(\varepsilon_1)=-\frac{1}{\mathrm{m_1}}\log(N_1)-\frac{\log(\mathrm{A_1})}{\mathrm{m_1}} \tag{35}$$

$-\frac{1}{\mathrm{m_1}}$ and $-\frac{\log(\mathrm{A_1})}{\mathrm{m_1}}$ are coefficients of $\log(\varepsilon_1)$ and $\log(N_1)$ linear function, see **FIGURE 3**. Hence, $\mathrm{A_1}$ and $\mathrm{m_1}$ can be obtained from S(strain)-N physical test data.

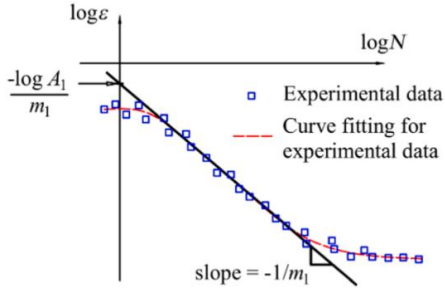

FIGURE 3. Theoretical and fitting curves of log(ε)-log(N) relationship (Nguyen, et al., 2021).

In phase II, to obtain the fatigue iteration parameters $\mathrm{A_2}$, $\mathrm{m_2}$, the Paris law is applied:

$$\frac{da}{dN}=C\Delta K^{\mathrm{M}} \tag{36}$$

Where a denotes the crack length, N denotes the number of loading cycles, and ΔK represents the stress intensity factor range. C and M denote material constants for the Paris equation. The fatigue iteration parameter m_2 is derived from the material constant M for the Paris equation:

$$m_2=M \tag{37}$$

Notice that A_2 cannot be derived from the Paris law directly. Hence, a trial fatigue simulation with a trial value $A_2^{'}$ needs to be operated. In the trial simulation, a crack growth rate $(da/dN)^{'}$ is predicted, while the real crack growth rate da/dN is derived from the physical experiment. Therefore, the calibrated value for A_2 is calculated by:

$$A_2=A_2^{'}\frac{da/dN}{(da/dN)^{'}} \tag{38}$$

Notice that m_1, A_1 and m_2 are independent of the horizon size, while the fatigue parameter A_2 is dependent on the horizon size. According to Silling's research (Silling and Askari, 2014), the relationship between the parameter A_2 and the horizon size δ is presented as:

$$A_2(\delta)=\widehat{A}_2\delta^{(m_2-2)/2} \tag{39}$$

Where $\widehat{A}_2$ is independent of δ.

As for the transition from phase I to phase II, for a particular material point x, if any material points within its horizon have the damage index $\phi < \phi_0$, point x is in phase I; if the damage index exceeds the critical damage index ϕ_0, point x is in phase II. According to Nguyen's research (Nguyen, et al., 2021), the empirical value ϕ_0=0.398 is applied to decide the transition from phase I to phase II.

As for the transition from phase II to phase III, if any bond strain s_{ij} exceeds the critical bond strain s_c, the structure turns to the rapid crack growth phase (phase III), then Equation (8) is applied to measure the bond breaking.

It should be noted that most of the S-N curves applied in F-BPD are in the form of strain cycles (Silling and Askari, 2014, Zhang, et al., 2016, Hu and Madenci, 2017, Jung and Seok, 2017, Han and Chen, 2020, Sajith, et al., 2020, Bang, et al., 2021, Nguyen,

et al., 2021, Bang and Ince, 2022, Li, et al., 2022), while most of the concrete S-N curves are in the form of stress cycles (Aas-Jakobsen, 1970, Tepfers and Kutti, 1979, Hsu, 1981, Saucedo, et al., 2013), which means under the framework of F-BPD, the concrete fatigue iteration parameters in phase I cannot be derived from concrete S-N curves directly. Besides, considering the fatigue failure performance of concrete, the F-BPD needs a proper cyclic failure criterion to measure the combined tension/compressive-shear fatigue failure in concrete. Hence, it is necessary to propose a novel fatigue model with a novel cyclic failure criterion for concrete fatigue failure.

3.2. A Novel fatigue model under Cosserat peridynamic framework.

This study proposes a novel fatigue model under Cosserat peridynamic framework (F-CPD) for concrete fatigue failure. In this model, to measure the combined tension/compressive-shear concrete fatigue failure, a novel cyclic bond failure criterion is defined from the Bresler-Pister criterion. The novel concrete fatigue failure model consists of three phases: the crack nucleation phase (phase I), the crack growth phase (phase II), and the rapid crack growth phase (phase III).

In F-CPD, each bond is subjected to both normal and tangential effects for a given bond ξ connecting material points x_1 and x_2, the equivalent cyclic bond force is defined as follows:

$$f_{\mathrm{bn}}=f_{1\mathrm{n}} \tag{40}$$

$$f_{\mathrm{bt}}=\beta_0\sqrt{(f_{1\mathrm{t}})^2+(\frac{\mathrm{M}_1}{|\xi|})^2} \tag{41}$$

It is assumed that each bond is regarded as a fictitious micro-beam subjected to tensile/compressive-shear effects, hence, every bond is affected by normal and tangential actions. The axial force component $f_{1\mathrm{n}}$ is regarded as the equivalent axial bond force f_{bn} in the bond between material point 1 and 2. f_{bt} is the equivalent tangential bond force acted by both tangential force component $f_{1\mathrm{t}}$ and pairwise moment M_1.

Considering that the tangential effect deforms and rotates the bond, only the effect on

the deformation part should be considered. Hence, the empirical coefficient β_0 is introduced to regulate the tangential effect (β_0 = 0.3 is appropriate in this study).

To derive the novel cyclic bond failure criterion, the Bresler-Pister criterion is introduced. Bresler-Pister criterion was proposed by Bresler (Bresler and Pister, 1958) in 1958, measuring the combined tension/compressive-shear failure in concrete beams. In this criterion, the normal octahedral stress σ_{oct} and tangential octahedral stress τ_{oct} are applied to measure the tension/compression-shear strength:

$$\frac{\tau_{oct}}{\sigma_0} = -1.16\frac{\sigma_{oct}}{\sigma_0} + 0.086 \tag{42}$$

$$\sigma_{oct} = \frac{1}{3}(\sigma_x + \sigma_y) \tag{43}$$

$$\tau_{oct} = \frac{1}{3}\sqrt{(\sigma_x - \sigma_y)^2 + \sigma_x^2 + \sigma_y^2 + 6\tau_{xy}^2} \tag{44}$$

Where σ_0 is the compressive strength. Take the plane stress condition for example. The criterion is expressed as follows:

$$\frac{\tau_{xy}}{\sigma_0} = \sqrt{0.011094 - 0.09976\left(\frac{\sigma_x}{\sigma_0} + \frac{\sigma_y}{\sigma_0}\right) - 0.10907\left[\left(\frac{\sigma_x}{\sigma_0}\right)^2 + \left(\frac{\sigma_y}{\sigma_0}\right)^2\right] + 0.78187\left(\frac{\sigma_x}{\sigma_0}\right)\left(\frac{\sigma_y}{\sigma_0}\right)} \tag{45}$$

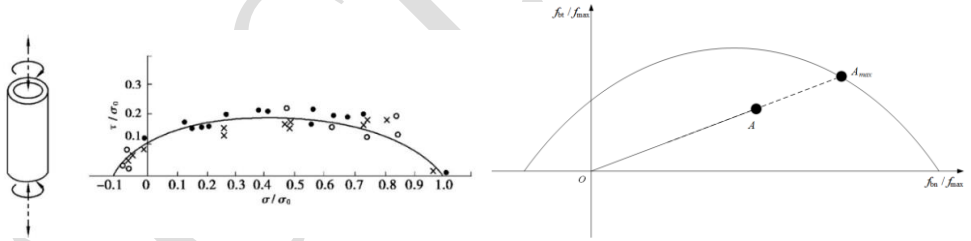

(a) (b)

FIGURE 4. (a) Relation curve of tensile/compression-shear zone of the beam and test points; (b) Relation curve of tensile/compression-shear zone of the bond.

FIGURE 4(a) shows the envelope of beam strength, the positive side of the σ/σ_0 axis means compression. When the point falls outside the envelope, the beam is damaged. In F-CPD, each bond is assumed to be a fictitious micro concrete beam subjected to combined tensile/compressive shear effects, and Equation (45) is rewritten as:

$$\frac{f_{bt}}{f_{max}} = \sqrt{0.011094 - 0.09976\frac{f_{bn}}{f_{max}} - 0.10907\left(\frac{f_{bn}}{f_{max}}\right)^2} \tag{46}$$

Where $f_{max} = s_{crc}c$, s_{crc} is the maximum compressive strain of the bond, the relation

curve of the tensile/compression-shear zone of the bond is obtained. In **FIGURE 4** (b), for a given bond ξ, if the bond failure state lies in point *A*, the cyclic bond failure state is expressed as:

$$S_{\mathrm{A}}=(1-R)\frac{\mathrm{OA}}{\mathrm{OA}_{\max}} \tag{47}$$

Where R is the load ratio (R=$\mathrm{P}_{\max}$/$\mathrm{P}_{\min}$). In F-CPD, the cyclic process is replaced by a quasi-static failure process, hence, the load ratio R is introduced to consider the cyclic effects.

For each bond, the remaining life $\lambda\ (x, \xi, N)$ is defined as:

$$\lambda=\begin{cases} \lambda_{ij}^{N=0}=1, \quad \frac{d\lambda_{ij}^{N}}{dN}=-\mathrm{A}_1\left(S_{ij}^{N}\right)^{\mathrm{m}_1} \text{ when } \mathrm{A}_1>0, \ \ \mathrm{m}_1>0 \text{ for phase I} \\ \lambda_{ij}^{N=0}=1, \quad \frac{d\lambda_{ij}^{N}}{dN}=-\mathrm{A}_2\left(S_{ij}^{N}\right)^{\mathrm{m}_2} \text{ when } \mathrm{A}_2>0, \ \ \mathrm{m}_2>0 \text{ for phase II} \end{cases} \tag{48}$$

To obtain the fatigue iteration parameter A_1 and m_1 in phase I, The S-N curve for concrete is introduced. Aas-Jakobsen (Aas-Jakobsen, 1970) et al. proposed a traditional $S_{\max}$-N curve, in which the cyclic stress ratio $R=\sigma_{\min}/\sigma_{\max}$ is considered:

$$S_{\max}=\frac{\sigma_{\max}}{f_0}=1-\beta(1-R)\log N \tag{49}$$

Where $\sigma_{\min}$, $\sigma_{\max}$ denote the minimum and the maximum stresses, respectively. f_0 denotes the static reference strength, β denotes the material parameter, calibrated to 0.0685 according to Tepfers' research (Tepfers and Kutti, 1979).

Considering a bond ξ_1 has the largest cyclic bond failure state S_1 in the body, then the bond ξ_1 will firstly be broken, compute the corresponding cycle N_1:

$$N_1=\frac{1}{\mathrm{A}_1 S_1^{\mathrm{m}_1}} \tag{50}$$

Take the log of both sides of Equation (50):

$$\log(S_1)=-\frac{1}{\mathrm{m}_1}\log(N_1)-\frac{\log(\mathrm{A}_1)}{\mathrm{m}_1} \tag{51}$$

Based on the $S_{\max}$-N curve of concrete proposed by Aas-Jakobsen (Aas-Jakobsen, 1970), the log(S)-log(N) curve is plotted as:

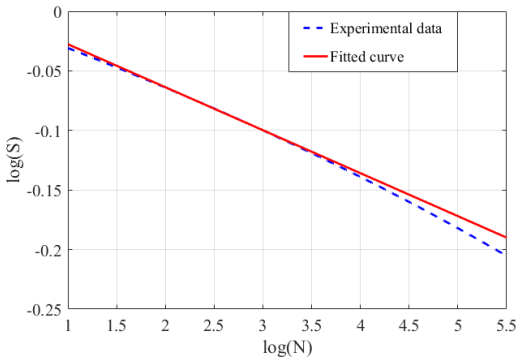

FIGURE 5. Theoretical and fitting curves of log(*S*)-log(*N*) relationship in the present model.

In **FIGURE 5**, an oblique line fits the theoretical log(*S*)-log(*N*) relationship. Hence, the slope and the intersection of the slope with the log(*S*) axis are equal to $-\frac{1}{m_1}$ and $-\frac{\log(A_1)}{m_1}$, respectively. Hence, the fatigue iteration parameters m_1 and A_1 are derived.

To derive the fatigue iteration parameters A_2, m_2 in phase II, the concrete Paris law is applied. The classical equations, including S(stress)-N curve and Paris law modified by Bazant (Bazant and Xu, 1991) are used to obtain the fatigue iteration parameters, which are widely mentioned in concrete failure research (Kim and Kim, 1999, Gaedicke, et al., 2009, Chen, et al., 2013, Bhowmik and Ray, 2018, Chen, et al., 2019). The size-adjusted Paris law for concrete is written as:

$$\frac{\Delta a}{\Delta N}=C\left[\frac{\Delta K_I}{K_{Ic}}\right]^n \tag{52}$$

In which ΔK_I is the amplitude of the stress intensity factor, K_{Ic} is the critical value of the stress intensity factor. The fatigue parameter m_2 is obtained from the material constant M for the Paris equation:

$$m_2=n \tag{53}$$

the remaining life $\lambda(x, \boldsymbol{\xi}, N)$ in the phase II is defined as:

$$\lambda_{ij}^{N=0}=1, \quad \frac{d\lambda_{ij}^N}{dN}=-A_2\left(S_{ij}^N\right)^{m_2} \tag{54}$$

The fatigue parameter A_2 cannot be calculated directly from Equation (52), and a trial peridynamic fatigue simulation with an arbitrary $A_2^{'}$ is needed. Then, a trial crack growth rate $(da/dN)^{'}$ is obtained, while the real crack growth rate da/dN is obtained by physical experiment, the calibrated value for A_2 in the present model is calculated as Equation (38). The fatigue parameters m_1, A_1 and m_2 are independent of the

horizon size, the fatigue parameter A_2 is dependent on the horizon size. The relationship between the parameter A_2 and the horizon size δ is presented as Equation (39).

Similar to F-BPD, phase transition conditions are necessary for F-CPD. For a given material point x, if all the material points within the horizon have the damage index $\phi < \phi_0$, then the point x is in phase I, if the damage index exceeds the critical damage index ϕ_0, then the point x is in phase II.

As for the transition from phase II to phase III, suppose a given bond ξ, the cyclic bond failure state lies in point *A*, refer to **FIGURE 4**(b). If point *A* is inside the envelope of the relation curve, the cyclic bond failure state is obtained, and the fatigue crack propagation is operated; if point *A* exceeds the envelope ($\frac{OA}{OA_{max}} \geq 1$) the fatigue simulation stops, and the rapid crack growth phase (phase Ⅲ) is used. In phase Ⅲ, the bond is broken if $\frac{OA}{OA_{max}} \geq 1$.

4. Numerical simulations

4.1. The fatigue test of the concrete three-point-bend beam.

In this section, mode I fatigue damage on the 2D model is predicted, considering a 2D concrete beam with sizes of 406.4mm×152.4mm×38.1mm, and the length of the pre-existing notch is 40mm. The maximum measured load for monotonic loading is P_{max}=5182N, the average fatigue life test result is N= 983, load ratio R = 0 (the load minimum is zero, and the load maximum is equal to 80 percent of the monotonic peak load P_{max}). In this section, the effects of thickness are not considered. The observed fatigue crack patterns are on the surface. Hence, the plane stress condition is considered. The physical parameters are applied: modulus of elasticity E=27.12GPa, the Poisson's ratio v=0.2, the limit stretch $s_c = 2.7926\times10^{-5}$, the concrete tensile strength f_t=2.86MPa.

In the numerical simulation, a square block is formed to apply fatigue load, see **FIGURE 6**. The concrete beam is discretized into 14970 material points, the discretized scale is 0.203mm, and the horizon size is δ=3.015·dx=0.612045mm. The Cosserat shear

modulus G_c=0.5G=6.408×10^9Pa (G is the shear modulus: G=$\frac{E}{2(1+v)}$) and the internal length is l_c=0.1mm.

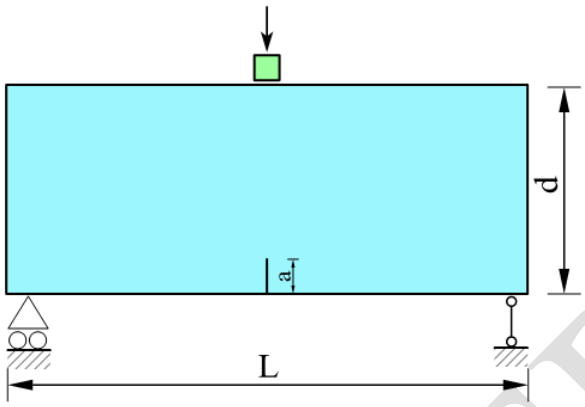

FIGURE 6. Initial configuration

Refer to Equations (46) and (48), the fatigue parameters (A_1, m_1) for phase I are obtained as:

$$A_1=0.1492$$

$$m_1=21.7391$$

The fatigue parameter m_2=9.27 is obtained from the physical experiments in Bažant's research (Bazant and Xu, 1991), a trial value $A_{2(trial)}$=2.0 is applied to obtain the trial fatigue crack growth rate $(da/dN)_{(trial)}$, to compare the trial and experimental data, the final $A_2 = 2.65$ is derived. Further numerical experiments are based on fatigue parameters in section 4.1 to avoid re-calculation of fatigue parameters due to the different concrete materials.

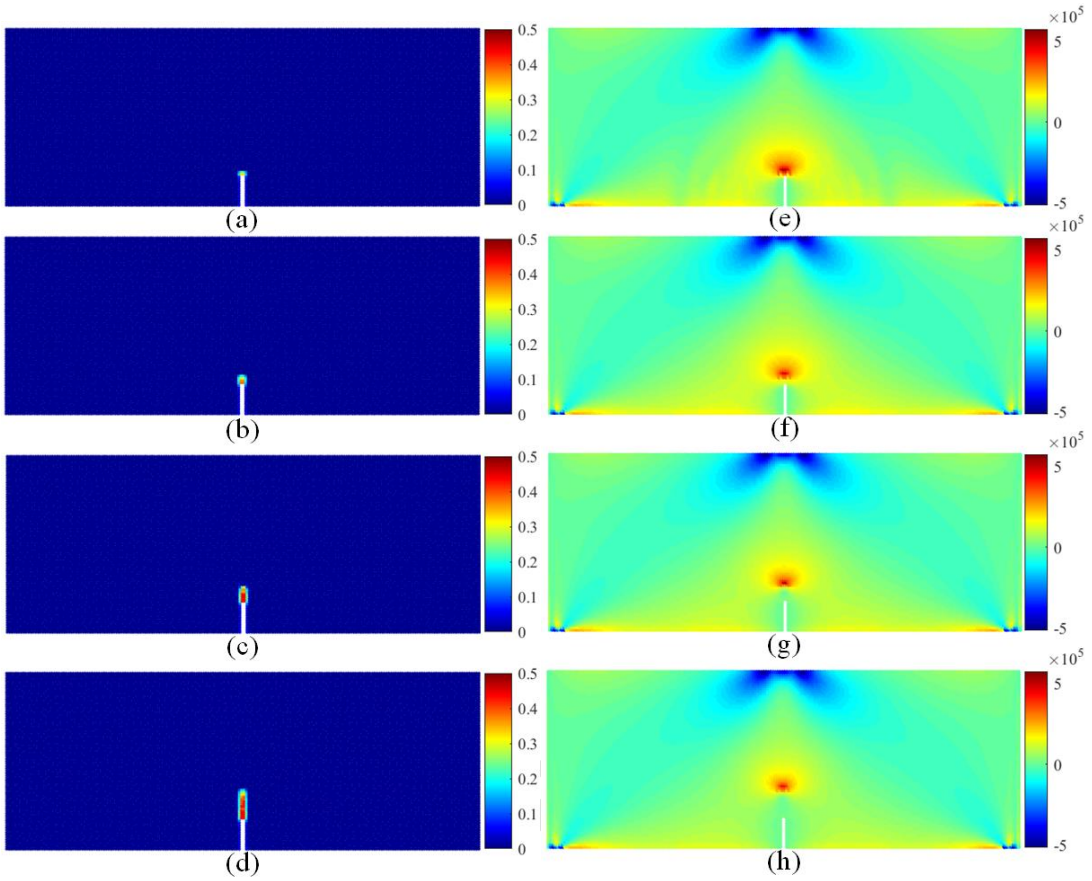

FIGURE 7. The damage evolution process of the concrete three-point-bend beam with the fatigue loading in cycles: (a)25; (b)500; (c)750; (d)1000, and the stress distribution in σ_{xx} in cycles: (e)25; (f)500; (g)750; (h)1000.

In **FIGURE 7** (a)-(d), mode I fatigue crack pattern is predicted. Notice that the damage areas initiate at the constraint due to the stress concentration. The crack tip begins to extend at cycle = 25 and spreads to 1/3 of the width in cycle = 1000. **FIGURE 7** (e)-(h) shows the peridynamic stress (Li, et al., 2022) distribution in σ_{xx} (the positive value indicates tension). It is observed that the stress concentration area locates at the crack tip during fatigue crack propagation.

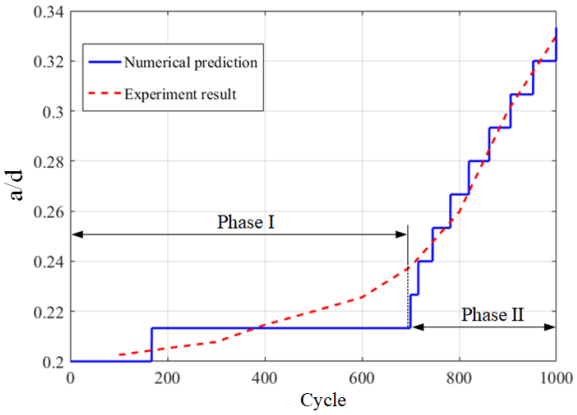

FIGURE 8. Numerical and physical relative crack length a/d with load cycles.

In **FIGURE 8**, the numerical relative crack length curve generally agrees with the physical experiment (Bazant and Xu, 1991). As for the numerical curve divided into phase I and phase II, in phase I, the crack tip extends to a/d= 0.2133. With the cyclic load applied, damage accumulates at the crack tip and forms the plateau of the numerical curve. When the damage index φ at the crack tip exceeds 0.398, fatigue crack propagation is transformed into phase II, and a steady fatigue crack propagation occurs, corresponding to the ascending part of the numerical curve. The final predicted fatigue life is N_p=1000(cycles), and the relative error of the final fatigue life is obtained as:

$$\text{error}(\%)=\frac{N_p-N_e}{N_e}\times 100=1.7\%$$

4.2. The uniaxial compressive concrete fatigue test.

This section predicts a mixed mode I-II fatigue crack pattern in 2D conditions. According to Viswanath's experiment (Viswanath, et al., 2021), see **FIGURE 9** (a), a rectangular plate is applied to investigate the compressive-shear concrete fatigue failure in 2D conditions. Consider a 101.6×203.2mm rectangular plate. See **FIGURE 9** (b). The plate is subjected to cyclic loading with maximum loading P_{max} = 4736N.

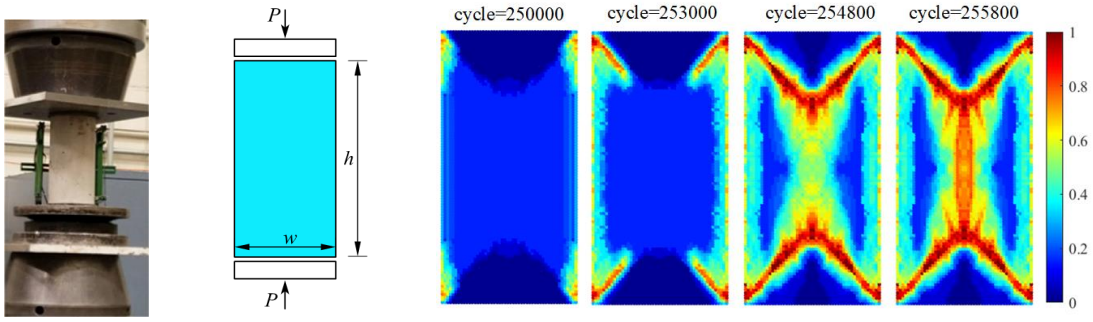

(a) (b) (c)

FIGURE 9(a) Fatigue loading process(Viswanath, et al., 2021); (b) initial configuration; (c) damage evolution process of uniaxial compressive fatigue test in the homogeneous group.

In the numerical simulation, two rigid blocks are separately formed at the upper and lower ends of the plate, which come into contact with the rectangular plate as uniaxial compressions. The sample is divided into 5000 points. The discretized scale is 0.203mm, and the horizon size is δ=3.015·dx=0.612045mm. The Cosserat shear modulus G_c=0.5G=6.408×10^9Pa, and the internal length is l_c=0.1mm.

In FIGURE 9 (c), damage initiates from the angular boundaries of the plate, then intersects and extends vertically into the center of the plate, and finally, a symmetric X - shaped crack is formed. The Weibull distribution of the intensity of material points is introduced (Feng and Zhou, 2022) to simulate the heterogeneity of concrete materials. The probability density of the Weibull distribution is expressed as:

$$f_w(x)=\begin{cases}\frac{m_w}{\eta_w}\left(\frac{x}{\eta_w}\right)^{m_w-1}e^{-(x/\eta_w)^{m_w}} & x\geq 0\\ 0 & x<0\end{cases} \tag{55}$$

In which m_w is the shape parameter, η_w is the scale parameter. The random variable x represents the intensity of the material point.

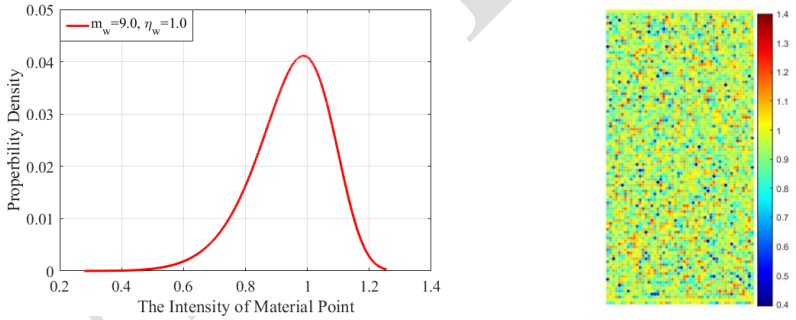

(a) (b)

FIGURE 10. (a) The probability density of the Weibull distribution f_w with m_w=9.0, η_w=1.0; (b) Weibull distribution of the intensity of material points.

The intensity of every material point is set to 1.0 in the homogeneous case to consider the heterogeneity of concrete. The Weibull distribution assigns each material point with an intensity $\Omega(i)$. See **FIGURE 10** (b). the intensity of the bond connecting material points x_i and x_j is denoted by 0.5($\Omega(i)$+ $\Omega(j)$). Hence, Equation (45) is rewritten as:

$$\lambda=\begin{cases}\lambda_{ij}^{N=0}=1, & \dfrac{d\lambda_{ij}^{N}}{dN}=-A_1\left(\dfrac{S_{ij}^{N}}{0.5(\Omega(i)+\Omega(j))}\right)^{m_1} \quad \text{when } A_1>0,\ m_1>0 \text{ for phase I}\\ \lambda_{ij}^{N=0}=1, & \dfrac{d\lambda_{ij}^{N}}{dN}=-A_2\left(\dfrac{S_{ij}^{N}}{0.5(\Omega(i)+\Omega(j))}\right)^{m_2} \quad \text{when } A_2>0,\ m_2>0 \text{ for phase II}\end{cases} \tag{53}$$

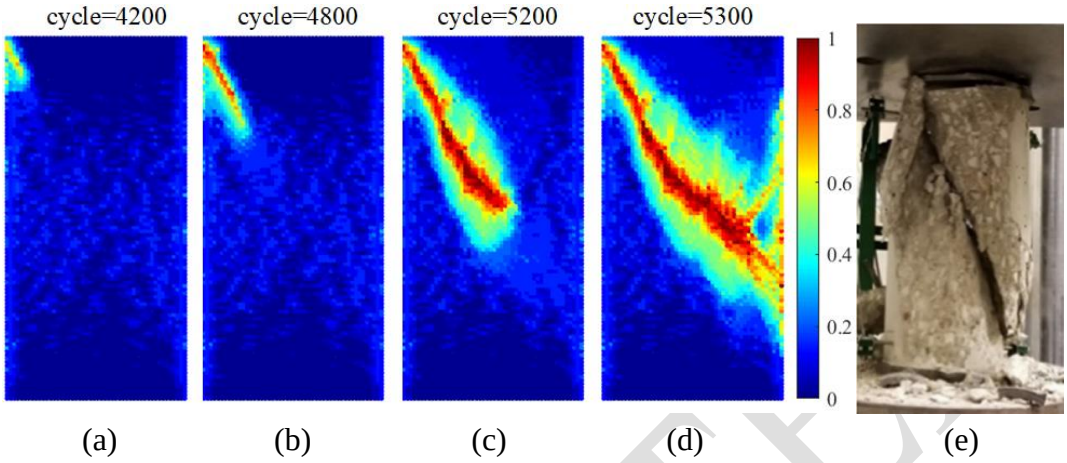

FIGURE 11. The damage evolution process of uniaxial compressive fatigue test with cycles: (a)4200; (b)4800; (c)5200; (d)5300; (e)experiment result

In **FIGURE 11** (a)-(d), the crack propagation is asymmetric in the non-homogeneous case. Crack initiates from the upper boundary and propagates to the lower boundary. The oblique cracks caused by compression-shear effects are similar to the experimental result in Viswanath's work (Viswanath, et al., 2021). Generally speaking, to tell the crack patterns that are persistent over samples, it is important to include the spread of experimental results. However, we searched for the compression fatigue experiments of concrete, there are rarely compressive fatigue experiments, only a few described the failure types due to the limitations of materials and experimental equipment.

Considering that the Cosserat shear modulus $G_c$and Cosserat internal length l_c describe the mechanical behavior of microstructure, the effect of G_c and l_c on crack patterns should be investigated.

4.2.1. The effect of Cosserat shear modulus G_c on fatigue crack pattern.

In this section, the effect of Cosserat shear modulus G_c is discussed, the internal length l_c is fixed to be $l_c = 1.0\times10^{-4}$m, G_c is set to vary from $0G$ to $0.5G$.

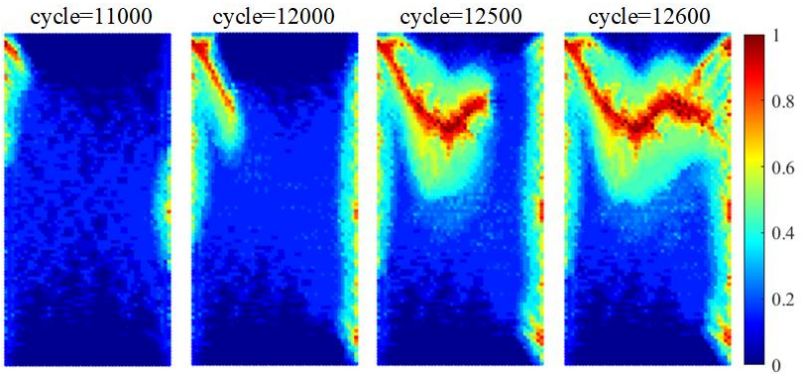
cycle=11000
cycle=12000
cycle=12500
cycle=12600
1
0.8
0.6
0.4
0.2
0

(a)

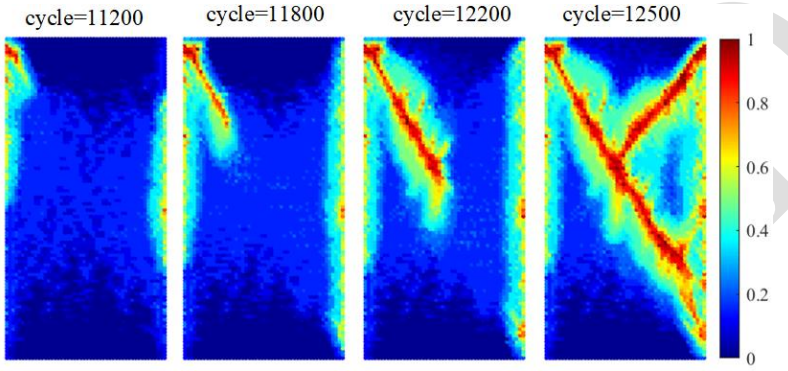
cycle=11200
cycle=11800
cycle=12200
cycle=12500
1
0.8
0.6
0.4
0.2
0

(b)

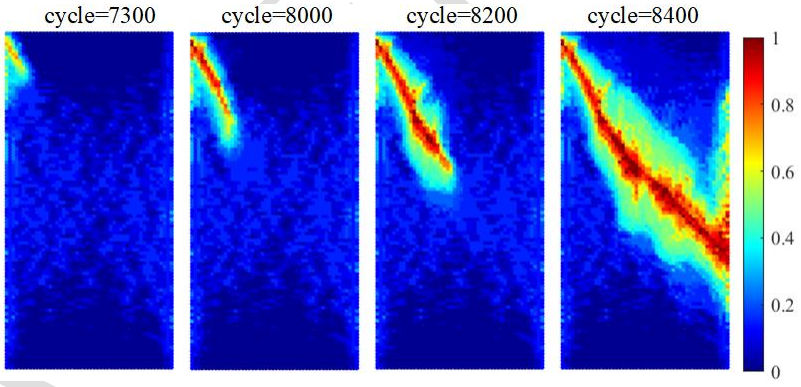
cycle=7300
cycle=8000
cycle=8200
cycle=8400
1
0.8
0.6
0.4
0.2
0

(c)

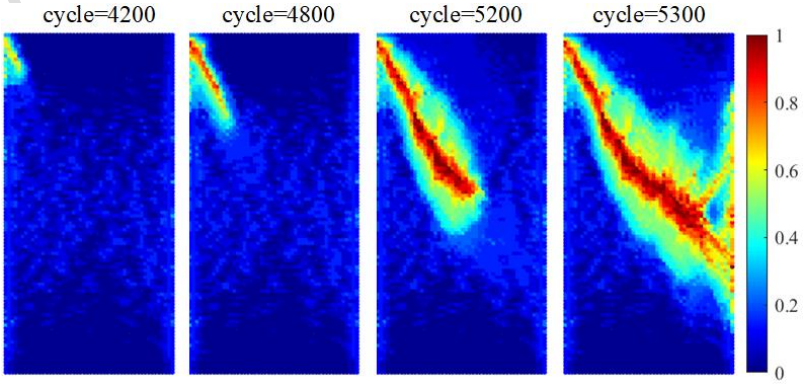
cycle=4200
cycle=4800
cycle=5200
cycle=5300
1
0.8
0.6
0.4
0.2
0

(d)

FIGURE 12. The damage evolution process of uniaxial compressive fatigue test with different G_c: (a) G_c=0G; (b) G_c=0.1G; (c) G_c=0.3G; (d) G_c=0.5G.

In **FIGURE 12**, the crack propagations are not synchronized among these groups, which means that fatigue crack patterns in the same propagation stage have different load cycles. Notice that the crack bifurcation occurs in groups (a) and (b), in group (b)-(d), with different G_c, the main direction of fatigue crack propagation does not change obviously, while the larger G_c corresponds to less fatigue life, which means the larger Cosserat shear modulus G_c accelerates the fatigue crack propagation process. To further investigate the effect of Cosserat shear modulus G_c on fatigue life, numerical groups with different G_c are designed to calculate the fatigue life distribution.

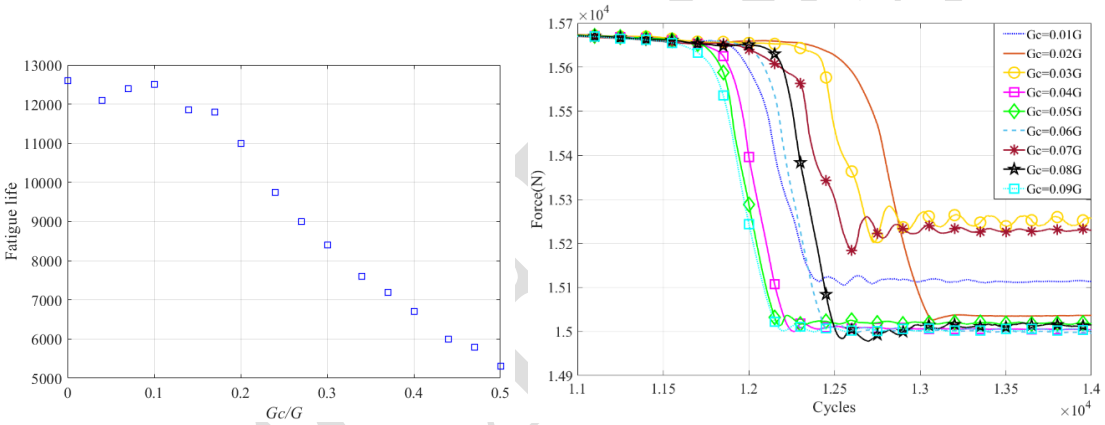

(a) (b)

FIGURE 13. (a)Fatigue life distribution of numerical groups with different Cosserat shear modulus G_c; (b) support force-cycle curves with different G_c.

In **FIGURE 13**(a), the effect of G_c on fatigue life works little between G_c=0 and G_c=0.1 G, as G_c increases and fatigue life decreases from 12500 to 5300. The finding that the larger Cosserat shear modulus G_c accelerates the fatigue crack propagation process is true between G_c=0.1G and G_c=0.5G. To investigate the oscillation between G_c=0 and G_c=0.1 G, several groups with different G_c are taken for further numerical simulation. The support force-cycle curves are plotted to measure the fatigue life of these groups, see **FIGURE 13**(b).

In **FIGURE 13**(b), Notice that the fatigue life of all groups falls within the interval of 12200 to 13000. The maximum difference in fatigue life is 7.1%. Different from the

findings in **FIGURE 13**(a), the group with a larger G_c does not correspond to smaller fatigue life, and the oscillation happens. After getting stable, curves show three states with different support forces corresponding to three crack patterns. For comparison, groups of G_c=0.01G, G_c=0.03G, G_c=0.05G are chosen to represent three crack patterns, respectively.

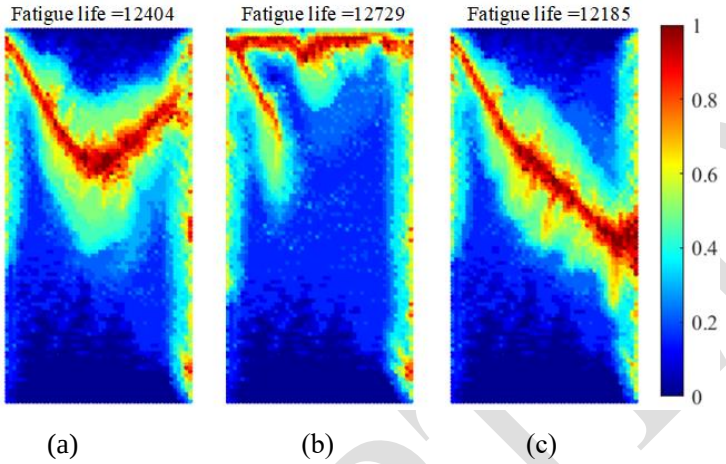

FIGURE 14. Crack patterns with different G_c: (a) G_c=0.01G; (b) G_c=0.03G; (c) G_c=0.05G.

In **FIGURE 14**, When G_c=0.01G, the crack initiates from the upper left corner of the specimen and spreads to the lower right, as extending to the middle of the specimen, the crack expands to the upper right; when G_c=0.03G, the crack initiates from the upper left corner of the specimen and spreads to the lower right. Meanwhile, the crack bifurcates from the initiation point and spreads horizontally to the right. As the bifurcation part propagates to the right boundary, fatigue failure occurs, and the oblique crack stop growing; when G_c=0.05G, the crack initiates from the upper left corner of the specimen and spreads to the lower right. As the crack propagates to the right boundary, fatigue failure occurs. In summary, G_c effects the fatigue crack patterns and makes the oscillation of fatigue life happens with G_c increases from 0 to 0.1G. The acceleration effect of G_c on fatigue crack propagation becomes obvious when G_c exceeds 0.1G.

4.2.2. The effect of Cosserat internal length l_c on fatigue crack pattern.

In this section, the effect of l_c is discussed, the Cosserat shear modulus G_c is fixed to be $G_c = 0.5\text{G}$, l_c is set to vary from 1.0×10^{-5}m to 5.0×10^{-4}m.

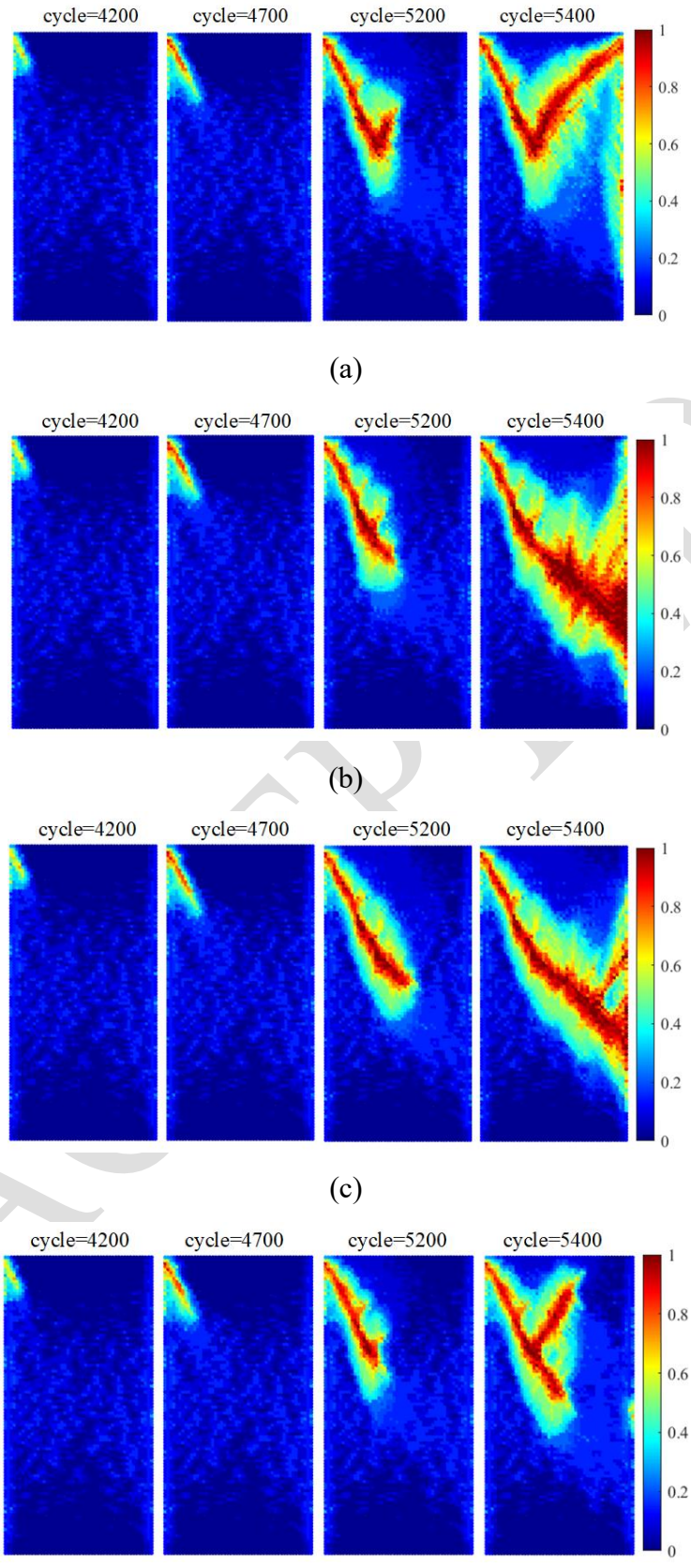

FIGURE 15. The damage evolution process of uniaxial compressive fatigue test with different l_c: (a) l_c=1.0×10^{-5}m; (b) l_c=5.0×10^{-5}m; (c) l_c=1.0×10^{-4}m; (d) l_c=5.0×10^{-4}m.

In **FIGURE 15,** fatigue life is similar in groups (a)-(c), and crack bifurcation exists in groups (a) and (d). In group (a), the main crack bifurcates at cycle=5200, while in group (d), the crack propagates simultaneously along the main and bifurcation directions. Groups (b) and (c) show the same crack patterns. Hence, different l_c reflects different microstructures and multiple crack patterns are predicted.

Notice that in the simulations, the width of the damaged region around the crack paths are very wide. On the one hand, concrete is composed of densely packed particles bound together by a matrix partially filling the interstitial pore space, connecting adjacent grains and forming cemented grain-to-grain contacts. Hence, the concrete fragments will form and spall near the crack surface when the fatigue fracture happens. On the other hand, the region with high damage value (damage > 0.8) is considered as the region where cracks occur. the damaged region around the crack paths means that the high damage areas (damage > 0.8) are vulnerable, and may peel off the specimen in the form of crushed grains, which makes the damaged region around the crack paths wide. The micro-crack forms in the other damage area (0< damage < 0.8) and reduces the intensity, but will not form the main crack.

4.2.3. Discussion about contact force between crack surfaces

As for the compressive fatigue test for concrete, the post-failure response should be discussed in detail, which means that it is important to consider the crack faces interaction, and the crack surface tracking method as well as the contact forces should be introduced.

To apply the contact force between crack faces, the crack surface should be traced. Unlike XFEM and other traditional methods, PD cannot directly represent the location and trend of fractures since the fractures are the accumulation of microdamage (Qin, et al., 2021). To deal with this difficulty, Qin et al. (Qin, et al., 2021) proposed a crack surface tracing and characterization method, in which the influence of the location of macrocracks on the damage value of material points is discussed. Hamarat et al. (Hamarat and Kaewunruen, 2023) proposed a PD damage assessment method, which defines that damage occurs between two close neighbor material points if they lose their direct and first-degree indirect contact, and the crack plane is created between those

material points. These two method could be chose to trace the crack surface.

As for the contact force, the contact model for peridynamics is usually local (short-range force model) (Wan, et al., 2020). Referring to the contact model of Macek (Macek and Silling, 2007) and Wan (Wan, et al., 2020), the normal contact force is expressed as:

$$\boldsymbol{f}_c^n = \min\left\{0, c_s\left(\frac{|\mathbf{y}_{(k)}-\mathbf{y}_{(i)}|}{d_c}-1\right)\right\}\cdot\mathbf{n}\cdot(1-R)\cdot\gamma \tag{54}$$

Where $\boldsymbol{f}_c^n$ is the contact force density vector imposed by material point $x_{(k)}$ on $x_{(i)}$, c_s is the spring constant harmonic mean value of material point i and k, according to Wan (Wan, et al., 2020), $c_s = \frac{2c_{(i)}c_{(j)}}{c_{(i)}+c_{(j)}}$. $\boldsymbol{n}$ is the unit normal vector pointing from $\boldsymbol{y}_{(i)}$ to $\boldsymbol{y}_{(k)}$. d_c is the representative distance, which is dl in this discussion. R is the load ratio. Considering that the interaction between crack surfaces could be weaker than the interaction between typical no-damage samples due to the high damage area in crack surfaces, an empirical coefficient γ is used to adjust the contact force, further parameter analysis will be carried out in the future work.

Notice that the tangential contact force is not discussed in Macek's work or Wan's work. As for the concrete material, the normal and tangential contact forces should obey Mohr-Coulomb criteria, which means the tangential contact force cannot exceed the maximum friction, hence, the tangential contact force is expressed as:

$$\boldsymbol{f}_c^t = \begin{cases} 0 & if\ \boldsymbol{f}_c^n = 0 \\ \min\left\{c_s\left(\frac{|\boldsymbol{y}_{(k)}-\boldsymbol{y}_{(i)}|}{d_c}-1\right)\cdot tan\phi,\ c_s\left(\frac{|\boldsymbol{y}_{(k)}-\boldsymbol{y}_{(i)}|}{d_c}-1\right)\right\}\cdot\boldsymbol{\tau}\cdot(1-R)\cdot\gamma & if\ \boldsymbol{f}_c^n \neq 0 \end{cases} \tag{55}$$

Where $\boldsymbol{\tau}$ is the unit tangential vector pointing from $\boldsymbol{y}_{(i)}$ to $\boldsymbol{y}_{(k)}$. $tan\phi$ is the frictional dilution.

Consider the amount of work required for further investigation, and the multiple choices of crack surface tracing methods, the discussion of describing contact forces between crack surfaces in the compressive fatigue tests needs further theoretical and numerical examinations, and is not enough to be added into this manuscript.

4.3. Biaxial compressive concrete fatigue test.

In this section, a biaxial compressive concrete fatigue test is performed. According

to Wang's experiments (Wang and Song, 2011), consider a concrete cube with a size of 200×200mm subjected to cyclic compression loads. In this section, the effects of thickness are not considered. The observed fatigue crack patterns are on the surface. Hence, the plane stress condition is considered.

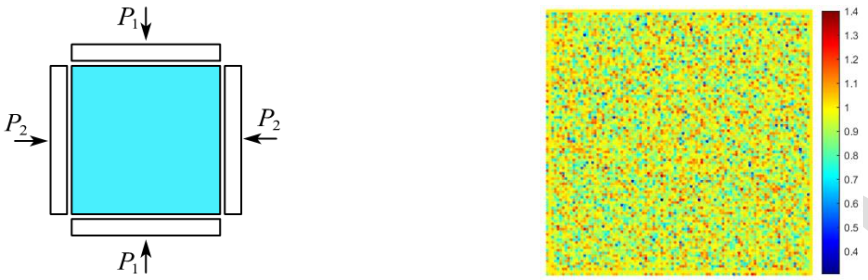

(a) (b)

FIGURE 16(a) initial configuration; (b) Weibull distribution of the intensity of material points.

In the numerical simulation, the upper and lower ends of the specimen are subjected to uniaxial cyclic load P_1, while the left and right ends of the specimen are subjected to cyclic loads P_2, which represents the action of confining pressure. The sample is divided into 10000 points, the discretized scale is 0.203mm, and the horizon size is δ=3.015·dx=0.612045mm. The Cosserat shear modulus G_c=0.5G=6.408×10^9Pa (G is the shear modulus: $G=\frac{E}{2(1+\nu)}$) and the internal length is l_c=0.1mm. Referring to Equation (52), the Weibull distribution of the intensity of material point is applied.

Four groups with different confining pressure are set to investigate the influence of confining pressure on fatigue failure. The uniaxial cyclic load P_1=7124N, the confining cyclic load P_2 varies from 0.1P_1 to 0.4P_1.

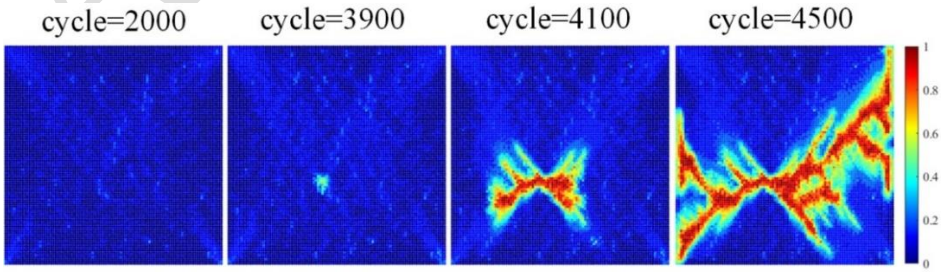

(a)

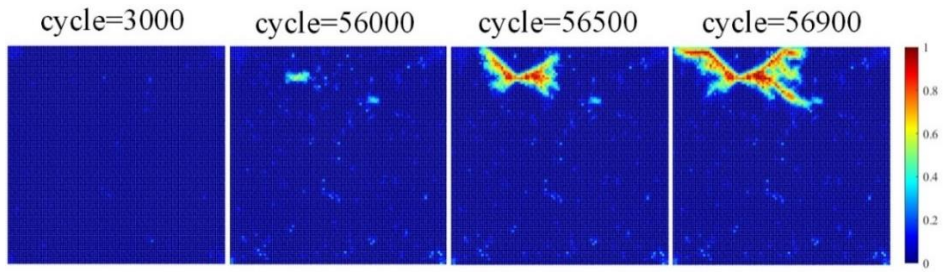

(b)

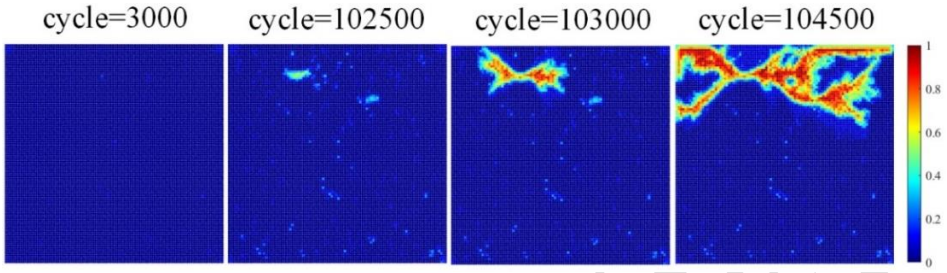

(c)

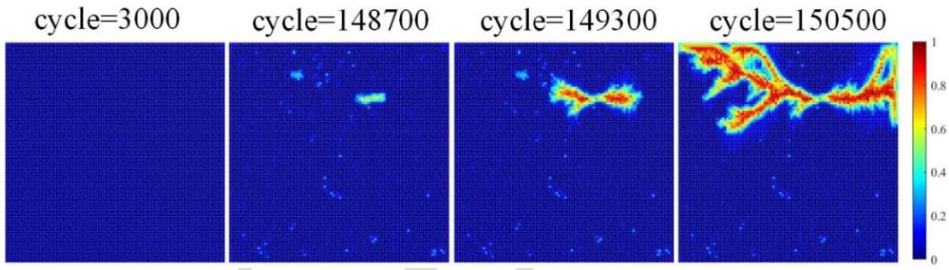

(d)

FIGURE 17. The damage evolution process of biaxial compressive fatigue test with different P_2: (a) $P_2=0.1P_1$; (b) $P_2=0.2P_1$; (c) $P_2=0.3P_1$; (d) $P_2=0.4P_1$.

In **FIGURE 17**, notice that minor defects appear in the interior of the plate and form macroscopic cracks with cycles. In group (a), unlike the other three groups, the crack presents a relatively dense oblique crack form. With the increase of confining pressure, the crack failure becomes localized. As the confining pressure increases, fatigue life increases obviously, which shows that the more significant confining pressure makes concrete structures more difficult to fail. Besides, the macroscopic cracks tend to develop horizontally with the confining pressure, corresponding to the physical experiment results (Wang and Song, 2011). In a word, the confining pressure limits the action of compression-shear effects.

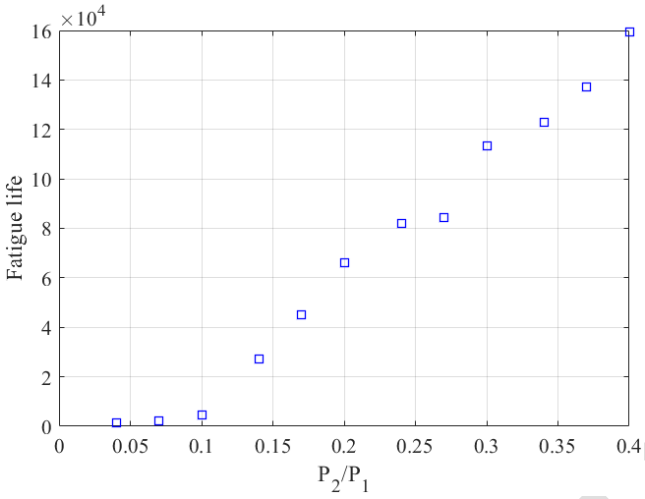

FIGURE 18. Fatigue life distribution of numerical groups with different confining cyclic load P_2.

To investigate the influence of confining pressure on fatigue life, numerical groups with different P_2 are designed to calculate the fatigue life distribution, see **FIGURE 18**. With P_2 increases, fatigue life increases from 4000 to 150000. The result shows that the confining pressure significantly impacts fatigue life, as observed in Wang's experiment.

5. Summary and Conclusion

This study proposes a novel fatigue model under Cosserat peridynamic framework for concrete fatigue cracking (F-CPD). The cyclic bond failure criterion derived from the Bresler-Pister criterion is defined to measure the combined tension/compressive-shear fatigue failure in concrete.

The benchmark of the fatigue test of a three-point-bend concrete beam is designed to validate the proposed model, and the mode I crack is simulated. The result shows that the crack length generally agrees with the experimental curve.

In the uniaxial compressive concrete fatigue test benchmark, the I-II mix mode crack is predicted in the non-homogeneous case. The fatigue iteration parameters are based on the calculated data in the mode I crack simulation benchmark, which should be revised with the result of the physics experiments in future work.

In the benchmark of the uniaxial compressive concrete fatigue test, the effects of G_c, l_c on fatigue crack patterns are discussed. Both the Cosserat shear modulus and the Cosserat internal length reflect the microstructures. Crack patterns reflect differently

with varied Cosserat shear modulus and the Cosserat internal length. As for the Cosserat shear modulus G_c, G_c affects the crack patterns and makes the oscillation of fatigue life happens with G_c increases from 0 to 0.1G. The acceleration effects of G_c on the fatigue crack propagation become obvious when G_c exceeds 0.1G.

In the biaxial compressive concrete fatigue test benchmark, the more significant confining pressure makes concrete structures more difficult to fail and makes the macroscopic cracks propagate horizontally.

Acknowledgment

The authors are pleased to acknowledge the support of this work by the National Natural Science Foundation of China through contract/grant numbers 12172263 and 11772237.

References

[1] J.L. Chaboche, P.M. Lesne, A non-linear continuous fatigue damage model, Fatigue. Fract. Eng. M., 11 (1988) 1-17.
[2] B. Sun, Z. Xu, An efficient numerical method for meso-scopic fatigue damage analysis of heterogeneous concrete, Constr. Build. Mater., 278 (2021) 122395.
[3] P.B. Cachim, J.A. Figueiras, P.A.A. Pereira, Numerical modelling of fibre-reinforced concrete fatigue in bending, Int. J. Fatigue, 24 (2002) 381-387.
[4] K. Aas-Jakobsen, Fatigue of concrete beams and columns, Division of Concrete Structures, Norwegian Inst. of Technology, University …1970.
[5] R. Tepfers, T. Kutti, Fatigue strength of plain, ordinary, and lightweight concrete, J. ACI., 76 (1979) 635-652.
[6] T.T. Hsu, Fatigue of plain concrete, Journal Proceedings, 1981, pp. 292-305.
[7] L. Saucedo, C.Y. Rena, A. Medeiros, X. Zhang, G. Ruiz, A probabilistic fatigue model based on the initial distribution to consider frequency effect in plain and fiber reinforced concrete, Int. J. Fatigue, 48 (2013) 308-318.
[8] M. Baluch, A. Qureshy, A. Azad, Fatigue crack propagation in plain concrete, Fracture of Concrete and Rock: SEM-RILEM International Conference June 17–19, 1987, Houston, Texas, USA, Springer, 1989, pp. 80-87.
[9] P.C. Perdikaris, A. Calomino, Kinetics of crack growth in plain concrete, Fracture of Concrete and Rock: SEM-RILEM International Conference June 17–19, 1987, Houston, Texas, USA, Springer, 1989, pp. 64-69.
[10] R.G. Forman, V. Kearney, R. Engle, Numerical analysis of crack propagation in cyclic-loaded structures, (1967).
[11] W. Elber, Einfluß der plastischen Zone auf die Rißausbreitung unter Schwingbelastung/Effect of the plastic zone on the crack propagation under cyclic loads/Influence de la zone plastique sur l 'extension des fissures sous efforts alternes,

Mater. Test., 12 (1970) 189-193.
[12] M. Klesnil, P. Lukáš, Influence of strength and stress history on growth and stabilisation of fatigue cracks, Eng. Fract. Mech., 4 (1972) 77-92.
[13] E. Priddle, Some equations describing the constant amplitude fatigue crack propagation characteristics of a mild steel. Berkeley Nuclear Laboratories, 1972, RD/B, 1972.
[14] Z.P. Bazant, K. Xu, Size effect in fatigue fracture of concrete, ACI Mater. J., 88 (1991) 390-399.
[15] T. Sain, J.C. Kishen, Probabilistic assessment of fatigue crack growth in concrete, Int. J. Fatigue, 30 (2008) 2156-2164.
[16] A. Carpinteri, A. Spagnoli, S. Vantadori, A multifractal analysis of fatigue crack growth and its application to concrete, Eng. Fract. Mech., 77 (2010) 974-984.
[17] S. Ray, J.C. Kishen, Fatigue crack propagation model and size effect in concrete using dimensional analysis, Mech. Mater., 43 (2011) 75-86.
[18] S. Ray, J. Chandra Kishen, Fatigue crack growth due to overloads in plain concrete using scaling laws, Sadhana, 37 (2012) 107-124.
[19] A. Hillerborg, M. Modéer, P.-E. Petersson, Analysis of crack formation and crack growth in concrete by means of fracture mechanics and finite elements, Cem. Concr. Res., 6 (1976) 773-781.
[20] D.A. Hordijk, Local approach to fatigue of concrete, (1993).
[21] B. Yang, S. Mall, K. Ravi-Chandar, A cohesive zone model for fatigue crack growth in quasibrittle materials, Int. J. Solids Struct., 38 (2001) 3927-3944.
[22] Z. Ding, D. Feng, X. Ren, J. Wang, Physically based constitutive modeling of concrete fatigue and practical numerical method for cyclic loading simulation, Eng. Fail. Anal., 101 (2019) 230-242.
[23] J. Marigo, Modelling of brittle and fatigue damage for elastic material by growth of microvoids, Eng. Fract. Mech., 21 (1985) 861-874.
[24] E. Papa, A. Taliercio, Anisotropic damage model for the multiaxial static and fatigue behaviour of plain concrete, Eng. Fract. Mech., 55 (1996) 163-179.
[25] S.H. Mai, F. Le-Corre, G. Forêt, B. Nedjar, A continuum damage modeling of quasi-static fatigue strength of plain concrete, Int. J. Fatigue, 37 (2012) 79-85.
[26] A.J. McEvily, R.P. Wei, Fracture mechanics and corrosion fatigue, Connecticut Univ Storrs Dept of Metallurgy, 1972.
[27] S. Pearson, The effect of mean stress on fatigue crack propagation in half-inch (12.7 mm) thick specimens of aluminium alloys of high and low fracture toughness, Eng. Fract. Mech., 4 (1972) 9-24.
[28] C. Branco, J. Radon, L. Culver, Influence of mean stress intensity on fatigue crack growth in an aluminium alloy, J. Mech. Eng. Sci., 17 (1975) 199-205.
[29] K. Miller, The two thresholds of fatigue behaviour, Fatigue. Fract. Eng. M., 16 (1993) 931-939.
[30] D. Pryl, J. Mikolášková, R. Pukl, Modeling fatigue damage of concrete, Key Eng. Mater., Trans Tech Publ, 2014, pp. 385-388.
[31] G. Lesiuk, M. Smolnicki, R. Mech, A. Ziety, C. Fragassa, Analysis of fatigue crack growth under mixed mode (I plus II) loading conditions in rail steel using CTS

specimen, Eng. Fail. Anal., 109 (2020).
[32] J.L. Wang, Y.Y. Yan, J. Yu, J.S. Wang, F.M. Du, Y.X. Yang, Fatigue evaluation of FV520B-I shrouded impeller blade with fatigue crack based on FEA and fracture mechanics, Eng. Fail. Anal., 115 (2020).
[33] S.R. Maitra, K. Reddy, L. Ramachandra, Numerical investigation of fatigue characteristics of concrete pavement, Int. J. Fract., 189 (2014) 181-193.
[34] Z. Ding, J. Li, A physically motivated model for fatigue damage of concrete, Int. J. Damage Mech., 27 (2018) 1192-1212.
[35] B. Wu, Z. Li, K. Tang, K. Wang, Microscopic multiple fatigue crack simulation and macroscopic damage evolution of concrete beam, Applied Sciences, 9 (2019) 4664.
[36] S.A. Silling, Reformulation of elasticity theory for discontinuities and long-range forces, Journal of the Mechanics and Physics of Solids, 48 (2000) 175-209.
[37] J. Wan, Z. Chen, X. Chu, H. Liu, Dependency of single-particle crushing patterns on discretization using peridynamics, Powder Technol., 366 (2020) 689-700.
[38] Z. Chen, X. Chu, Peridynamic modeling and simulation of fracture process in fiber-reinforced concrete, CMES- Comp. Model. Eng., 127 (2021) 241-272.
[39] Z. Chen, X. Chu, Numerical fracture analysis of fiber-reinforced concrete by using the cosserat peridynamic model, J. Peridyn. Nonlocal Model., (2022) 1-24.
[40] Z. Chen, X. Chu, Q. Duan, A micromorphic peridynamic model and the fracture simulations of quasi-brittle material, Eng. Fract. Mech., 271 (2022) 108631.
[41] K. Feng, X. Zhou, Peridynamic simulation of the mechanical responses and fracturing behaviors of granite subjected to uniaxial compression based on CT heterogeneous data, Eng Comput-Germany., (2022) 1-23.
[42] X. Guo, Z. Chen, X. Chu, J. Wan, A plane stress model of bond-based Cosserat peridynamics and the effects of material parameters on crack patterns, Eng. Anal. Boundary Elem., 123 (2021) 48-61.
[43] M.S. Breitenfeld, P.H. Geubelle, O. Weckner, S.A. Silling, Non-ordinary state-based peridynamic analysis of stationary crack problems, Comput. Methods Appl. Mech. Eng., 272 (2014) 233-250.
[44] E. Madenci, S. Oterkus, Ordinary state-based peridynamics for plastic deformation according to von Mises yield criteria with isotropic hardening, Journal of the Mechanics and Physics of Solids, 86 (2016) 192-219.
[45] W. Gerstle, N. Sau, S. Silling, Peridynamic modeling of concrete structures, Nucl. Eng. Des., 237 (2007) 1250-1258.
[46] N. Prakash, G.D. Seidel, A novel two-parameter linear elastic constitutive model for bond based peridynamics, 56th AIAA/ASCE/AHS/ASC Structures, Structural Dynamics, and Materials Conference, 2015.
[47] A. Yaghoobi, M.G. Chorzepa, Fracture analysis of fiber reinforced concrete structures in the micropolar peridynamic analysis framework, Eng. Fract. Mech., 169 (2017) 238-250.
[48] Q. Zhu, T. Ni, Peridynamic formulations enriched with bond rotation effects, Int. J. Eng. Sci., 121 (2017) 118-129.
[49] X. Zhou, Y. Wang, Y. Shou, M. Kou, A novel conjugated bond linear elastic model in bond-based peridynamics for fracture problems under dynamic loads, Eng. Fract.

Mech., 188 (2018) 151-183.
[50] Z. Chen, J. Wan, X. Chu, H. Liu, Two Cosserat peridynamic models and numerical simulation of crack propagation, Eng. Fract. Mech., 211 (2019) 341-361.
[51] V. Diana, S. Casolo, A bond-based micropolar peridynamic model with shear deformability: Elasticity, failure properties and initial yield domains, Int. J. Solids Struct., 160 (2019) 201-231.
[52] X. Huang, S. Li, Y. Jin, D. Yang, G. Su, X. He, Analysis on the influence of Poisson's ratio on brittle fracture by applying uni-bond dual-parameter peridynamic model, Eng. Fract. Mech., 222 (2019).
[53] X. Gu, Q. Zhang, A modified conjugated bond-based peridynamic analysis for impact failure of concrete gravity dam, Meccanica, 55 (2020) 547-566.
[54] V. Diana, Anisotropic Continuum-Molecular Models: A Unified Framework Based on Pair Potentials for Elasticity, Fracture and Diffusion-Type Problems, Arch. Comput. Methods Eng., 30 (2022) 1305-1344.
[55] S.A. Silling, A. Askari, Peridynamic model for fatigue cracking, Sandia National Lab.(SNL-NM), Albuquerque, NM (United States), 2014.
[56] G. Zhang, F. Bobaru, Modeling the Evolution of Fatigue Failure with Peridynamics, The Romanian Journal of Technical Sciences. Applied Mechanics, 61(1) (2016) 22-40.
[57] G. Zhang, Q. Le, A. Loghin, A. Subramaniyan, F. Bobaru, Validation of a peridynamic model for fatigue cracking, Eng. Fract. Mech., 162 (2016) 76-94.
[58] Y. Hu, E. Madenci, Peridynamics for fatigue life and residual strength prediction of composite laminates, Compos. Struct., 160 (2017) 169-184.
[59] J. Jung, J. Seok, Mixed-mode fatigue crack growth analysis using peridynamic approach, Int. J. Fatigue, 103 (2017) 591-603.
[60] C.T. Nguyen, S. Oterkus, E. Oterkus, An energy-based peridynamic model for fatigue cracking, Eng. Fract. Mech., 241 (2021) 107373.
[61] J. Han, W. Chen, An ordinary state-based peridynamic model for fatigue cracking of ferrite and pearlite wheel material, Applied Sciences, 10 (2020) 4325.
[62] T. Ni, M. Zaccariotto, U. Galvanetto, A peridynamic approach to simulating fatigue crack propagation in composite materials, Philos Trans A Math Phys Eng Sci, 381 (2023) 20210217.
[63] S. Sajith, K. Murthy, P. Robi, Experimental and numerical investigation of mixed mode fatigue crack growth models in aluminum 6061-T6, Int. J. Fatigue, 130 (2020) 105285.
[64] D. Bang, A. Ince, E. Oterkus, S. Oterkus, Crack growth modeling and simulation of a peridynamic fatigue model based on numerical and analytical solution approaches, Theor. Appl. Fract. Mech., 114 (2021) 103026.
[65] D. Bang, A. Ince, Integration of a peridynamic fatigue model with two-parameter crack driving force, Eng Comput-Germany., 38 (2022) 2859-2877.
[66] H. Li, Z. Hao, P. Li, X. Li, D. Zhang, A low cycle fatigue cracking simulation method of non-ordinary state-based peridynamics, Int. J. Fatigue, 156 (2022) 106638.
[67] B. Bresler, K.S. Pister, Strength of concrete under combined stresses, Journal Proceedings, 1958, pp. 321-345.
[68] S.A. Silling, E. Askari, A meshfree method based on the peridynamic model of

solid mechanics, Comput. Struct., 83 (2005) 1526-1535.
[69] H. Tang, Z. Hu, Application of the Cosserat continua to numerical studies on the properties of the materials, Mech. Adv. Mater. Struct., 24 (2017) 797-808.
[70] P. Trovalusci, R. Masiani, Non-linear micropolar and classical continua for anisotropic discontinuous materials, Int. J. Solids Struct., 40 (2003) 1281-1297.
[71] P. Trovalusci, M. Ostoja-Starzewski, M.L. De Bellis, A. Murrali, Scale-dependent homogenization of random composites as micropolar continua, Eur. J. Mech. A-Solid., 49 (2015) 396-407.
[72] Z. Chen, X. Chu, Numerical Fracture Analysis of Fiber-Reinforced Concrete by Using the Cosserat Peridynamic Model, Journal of Peridynamics and Nonlocal Modeling, 4 (2021) 88-111.
[73] R. Tepfers, T. Kutti, Fatigue strength of plain, ordinary, and lightweight concrete, Journal Proceedings, 1979, pp. 635-652.
[74] J.K. Kim, Y.Y. Kim, Fatigue crack growth of high-strength concrete in wedge-splitting test, Cem. Concr. Res., 29 (1999) 705-712.
[75] C. Gaedicke, J. Roesler, S. Shah, Fatigue crack growth prediction in concrete slabs, Int. J. Fatigue, 31 (2009) 1309-1317.
[76] Y. Chen, J. Zhou, L. Liu, M. Sun, The Study of Fatigue Crack Growth Rate When Consider the Impact of the Crack Tip Plastic Zone of the Concrete, Intell. Autom. Soft Comput., 19 (2013) 589-597.
[77] S. Bhowmik, S. Ray, An improved crack propagation model for plain concrete under fatigue loading, Eng. Fract. Mech., 191 (2018) 365-382.
[78] C. Chen, X. Chen, S. Guo, Experimental study on acoustic emission characteristic of fatigue crack growth of self‐compacting concrete, Struct. Control Health Monit., 26 (2019) e2332.
[79] S. Viswanath, J.M. LaFave, D.A. Kuchma, Concrete compressive strain behavior and magnitudes under uniaxial fatigue loading, Constr. Build. Mater., 296 (2021) 123718.
[80] M. Qin, D. Yang, W. Chen, X. Xia, Hydraulic fracturing network modeling based on peridynamics, Engineering Fracture Mechanics, 247 (2021).
[81] M. Hamarat, S. Kaewunruen, A novel damage assessment method in Peridynamic simulations, Applied Mathematical Modelling, 123 (2023) 274-294.
[82] R.W. Macek, S.A. Silling, Peridynamics via finite element analysis, Finite Elements in Analysis and Design, 43 (2007) 1169-1178.
[83] H. Wang, Y. Song, Fatigue capacity of plain concrete under fatigue loading with constant confined stress, Mater. Struct., 44 (2011) 253-262.